On the mechanistic difference between in-phase and out-of-phase thermo-mechanical fatigue crack growth

V. Norman[a,*], S. Stekovic[a], J. Jones[b], M. Whittaker[b], B. Grant[c]

[a] Division of Engineering Materials, Department of Management and Engineering, Linköping University, SE-58183 Linköping, Sweden
[b] Institute of Structural Materials, Swansea University, Swansea SA1 8EN, UK
[c] Rolls-Royce plc, Derby DE24 8BJ, UK

ARTICLE INFO

ABSTRACT

The crack driving mechanisms in a coarse grained nickel-base superalloy RR1000 when subjected to in- and out of phase thermo mechanical fatigue are investigated. It is found that the difference in fatigue crack growth rate between these two load conditions is accounted for by the different mechanical conditions at the crack tip region, rather than oxidation effects. This is based on digital image correlation and finite element analyses of the mechanical strain field at the crack tip, which demonstrate that in phase leads to larger crack tip deformation and crack opening. Notably, it is demonstrated that in- and out of phase crack growth rates coincide when correlated to the crack tip opening displacement.

1. Introduction

In recent years, there has been an increased awareness of the environmental impact of air travel. Therefore, it is of vital strategic importance to the aviation industry to reduce aero engine emissions, which is driven by the EU's Aviation Vision 2020 along with industrial competition [1].

A significant portion of these improvements are expected to come from new engine designs in term of gas turbine efficiency. Such an increase in efficiency of the gas turbine is usually achieved either by weight reductions or by increasing the combustion temperature as a result of fuel being burnt at temperatures approaching the stoichiometric value [2]. In either case, the material choice is of critical importance. Effectively, the modern criteria for selecting materials include requirements on high temperature fatigue and creep capabilities, as well as requirements on suitable environmental and corrosion resistant properties, which in the present context typically results in the employment of nickel base superalloys. The motivation of these strict criteria is that the gas turbine operation cycle imposes harsh alternating mechanical and thermal loads on the material during start up, take off, descent and shut down. Such thermo mechanical conditions have the potential to cause local stresses to peak at temperatures far below the flight cycle maximum, resulting in the nucleation and propagation of cracks; a phenomenon known as thermo mechanical fatigue (TMF).

In essence, TMF is a complex failure mechanism, caused by combined thermal and mechanical load cycles [3], but is not a novel phenomenon. Rather, it is well acknowledged to be the primary life limiting aspect for many engineering components exposed to elevated temperatures, such as parts in the combustion chamber, along with turbine blades and discs [4,5]. More precisely, the TMF process can be divided into an initiation and propagation stage, where this investigation addresses the latter. Only a very limited number of investigations have been conducted involving TMF crack growth experiments on nickel base superalloys, however, it has been established that the crack growth rate is highly dependent on the phase angle between the thermal and mechanical cycle, e.g. in (IP) and out of phase (OP) cycling [6–8]. This introduces new perspectives regarding the general crack growth mechanism in fatigue at elevated temperatures, which have been extensively studied in the past based on isothermal fatigue and dwell fatigue experiments [9–27]. In particular, based on crack growth experiments in air and vacuum [9–17], the general conclusion is that oxygen plays a significant role, possibly through one of a number of proposed mechanisms [16]. On top of this, some authors have argued that inelastic creep deformation and stress relaxation at the crack tip may influence the growth rate [7,11,12,14,15,19,20]. However, it is not yet known whether these mechanisms are able to account for the differences seen between IP and OP TMF crack growth experiments.

In view of the above investigations, three different kinds of mechanisms which potentially may account for the difference in OP and IP, are identified. Firstly, (i) it is suggested that crack closure effects
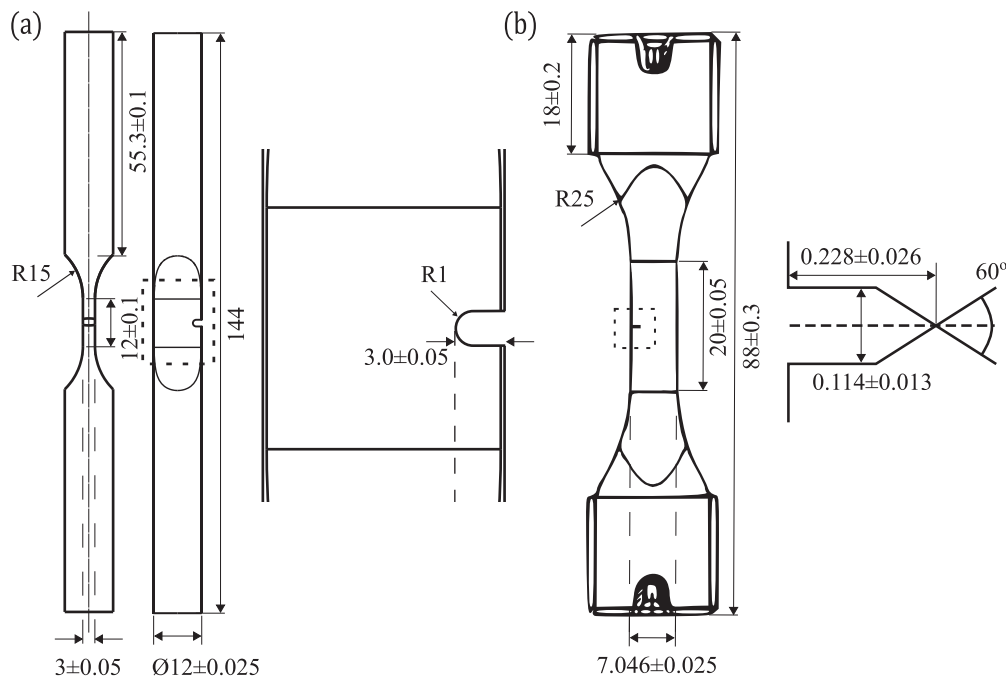

Fig. 1. (a) The single edge notched and (b) corner crack specimen geometry used for the TMF crack growth experiments.

may influence the crack growth rate depending on the thermo mechanical phase angle. For instance, recent studies [8,28–30] have demonstrated that variations in crack growth rate caused by altering the load ratio and temperature cycle are accounted for by compensating the stress intensity factor range or the cyclic J integral with respect to crack closure. Secondly, (ii) it is also expected that the different phase angles may induce different stress strain states in the crack tip, which may both explicitly and implicitly affect crack growth. For instance, different amount of inelastic crack tip deformation may occur depending on whether the cycle is OP or IP. Conversely, implicit effects such as the relation between the stress strain state at the crack tip and the diffusion of oxygen are also possible [9,10,16,31]. Accordingly, as the third and final category, (iii) it is also likely that aspects related to the material structure may account for the effect of phase angle, including the mentioned environment material interaction and potential crack tip phase transformations [11,32]. In other words, any potential material related weakening or toughening at the crack tip, dependent or independent of the atmosphere.

Even though fatigue crack growth mechanisms in nickel base superalloys under isothermal conditions have been extensively investigated in the past, there is at present a very limited understanding of the governing mechanisms under thermo mechanical load conditions, which is necessary for the efficient development of next generation gas turbine materials. Accordingly, the objective of this investigation is to render a better understanding of the mechanisms responsible for causing the difference in crack growth rate between IP and OP TMF load conditions. This is done by performing IP and OP TMF crack growth tests on a coarse grained nickel base superalloy RR1000, for which the potential mechanisms, including crack closure, crack tip deformation and oxidation effects, are investigated by in situ digital image correlation (DIC) and metallographic studies of interrupted tests. In this way, the mechanisms are identified and their contribution assessed by comparison of the IP and OP case. This has given new insights regarding general aspect of crack growth at elevated temperatures relevant for both isothermal and thermo mechanical load conditions.

2. Experimental and computational methods

2.1. Materials

RR1000 is a superalloy developed by Rolls Royce plc and is mainly used for discs in the rotative aero engine hot sections because of its excellent high temperature mechanical properties. The fine grained RR1000 has at least 25 °C increase in temperature capability over 720Li and an equivalent crack growth behaviour to coarse grained Waspaloy [33]. However, the need for increased engine efficiency and lower emissions has been driving towards higher pressure ratios and higher operation temperatures. Therefore, a coarse grained RR1000 has been developed to improve creep performance and fatigue crack growth resistance of these components [34].

Coarse grained RR1000 is processed by a powder metallurgy route and strengthened by Ni_3Al type gamma prime precipitates. The nominal chemical composition in wt% and details about the processing as well as the heat treatment of the alloy are given in reference [14]. The microstructure typically consists of grain sizes of ASTM 7 3 (32–125 μm). Apart from the gamma matrix and main strengthening secondary and tertiary gamma prime phases, the material also contains a dispersed sub micron phases such as MC carbides and M_3B_2 borides. Both gamma prime precipitates are distributed intergranularly with particle sizes ranging from 1 μm to 5 nm depending on the heat treatment and cooling rates [35,36].

2.2. Measurement of fatigue crack growth rates under thermo mechanical fatigue load conditions

The purpose with this test procedure is to assess the fatigue crack growth rate when subjected to thermo mechanical cycling, in contrast to standard fatigue crack growth tests during which the temperature is constant. As similar to conventional thermo mechanical fatigue (TMF) testing [3], the temperature varies with the same periodicity as the applied mechanical load with a given phase angle such as for instance 0 or 180 degrees, often denoted as in phase (IP) and out of phase (OP), respectively. As a consequence of the varying temperature, a distinction between the different causes of deformation in the tests specimen must be made, typically as

$$\varepsilon_e(t) = \varepsilon_{th}(t) + \varepsilon_{mech}(t) \tag{1}$$

where ε_e is the actual strain measured by an extensometer, ε_{th} is the thermal strain, *i.e.* the thermal expansion which varies with the temperature, and ε_{mech} is the mechanical strain whose origin is solely the applied force.

2.2.1. Specimen geometry

For the aforementioned purpose, the specimens used were notched in order to initiate a starting crack following a pre cracking procedure explained below. The specimen geometry is displayed in Fig. 1a. The grip section of the specimen was cylindrical with a diameter of 12 mm while the middle section had an approximately rectangular cross section with a thickness of 3 mm and a width of 12 mm. Nominally, the notch had a radius of 1 mm and a notch depth of 3.0 mm. The specimens were manufactured through turning and wire electrical discharge machining, without application of any additional surface finishing process.

2.2.2. Pre cracking procedure

A pre cracking procedure was conducted to initiate and propagate a starting crack to a reasonable length. Due to lack of experience, the pre cracking procedure was varied for the first specimens until an optimised procedure regarding minimal duration and applied stress, was established. For this reason, the procedure was not the same for most of the specimens. The load parameters and notch geometry employed for crack initiation are displayed in Table 1. Subsequent propagation to reach a reasonable starting crack length was done in a stepwise manner reducing the maximum stress with steps of 30 MPa in order to propagate through any eventual plastic zone caused by the previous maximum stress value. Regarding the test initiated at $\sigma_{max} = 210$ MPa and $R = -1$ (S3 and S5 in Table 1), these were subsequently propagated at 240 MPa, and then again at 210 MPa with R = 0 for the same reason prior to the actual test. At the end of the pre cracking procedure for each specimen, the crack had a length of about one millimetre. It should also be noted that one of the tests, S4 was initiated and propagated using the same temperature cycle as the actual test with the purpose of investigating the effect of a TMF initiated starting crack as similar to what is expected in a real component. Furthermore, the second test S2 was carried out with an alternative notch appearance, which however, did not decrease the duration of the pre crack procedure.

2.2.3. Test procedure

After having reached the desired starting crack length, the crack growth tests were conducted in both a IP and OP configuration, with a temperature cycle between 400 and 750 °C. The total cycle time was

Table 1
Information regarding the conducted crack growth tests and the associated pre cracking procedure.

Name	Test 400–750 °C R = 0	Crack initiation 25 °C 20 Hz	Notch geometry
S1	$\sigma_{max} = 250$ MPa IP	R = 0 $\sigma_{max} = 300$ MPa	
S2	$\sigma_{max} = 210$ MPa IP	R = 0 $\sigma_{max} = 300$ MPa	
S3	$\sigma_{max} = 210$ MPa OP	R = −1 $\sigma_{max} = 210$ MPa	
S4	$\sigma_{max} = 210$ MPa IP	400–750 °C R = −1 $\sigma_{max} = 240$ MPa	
S5	$\sigma_{max} = 210$ MPa IP	R = −1 $\sigma_{max} = 210$ MPa	

70 s divided into 35 s ramp up and down in temperature with a triangular wave shape. The mechanical load consisted of a prescribed stress with the same periodicity as the above cycle and a load ratio R equal to zero. A total number of five crack growth test were conducted as presented in Table 1.

2.2.4. Test set up

All tests and pre crack operations were conducted in an Instron 8801 servo hydraulic test machine equipped with an induction heating system including a cylindrical copper coil with its centre axis coinciding with the specimen centre axis. To even out the temperature distribution and assist cooling, compressed air flow directed towards the specimen through three nozzles was used, positioned circumferentially with equal angular spacing and the same distance to the specimen, as well as at the same vertical position as the notch. All tests were controlled and monitored using a dedicated TMF software developed by Instron, which automatically performs a pre test procedure, involving thermal stabilisation, thermal strain measurement and validation. In addition, an elastic modulus measurement program included in the software was run prior to the test on each specimen, measuring the elastic modulus at different constant temperatures using load cycles of ± 20 MPa, hence safely within the elastic range of the material. The strain was measured using an Instron extensometer 2632-055 with a gauge length L_e of 12.5 mm and the temperature was measured using a N type thermocouple spot welded in the centre of the side surface of the specimen, slightly beneath the expected crack path. After each test, it was verified that the thermocouple did not interfere with the crack path.

Before the start of the test series, a thermal profiling procedure was conducted in order to evaluate the temperature distribution on the specimen. For this purpose, a dummy specimen was tested to which six different N type thermocouples were attached at six different locations; three on each side evenly distributed along the axial centre line of the specimen. By monitoring the temperature at each thermocouple, the coil and air nozzles were adjusted in order to achieve a temperature difference less than 10 °C throughout the selected temperature cycle, as recommended by the TMF standard [3]. Evidently, the chosen configuration of the coil and air nozzles was not changed during the subsequent test series.

2.2.5. Crack length measurement method

The crack length as a function of number of cycles was determined using the compliance method in accordance with previous investigations involving the same or similar specimen geometry [29,37,38]. The method is based on the correlation between the crack length and the compliance or stiffness of the specimen, which is acquired from finite element simulations of the employed specimen geometry. The method is outlined in detail in [38] and is only briefly reproduced here.

A finite element model representing the specimen was set up using Abaqus CAE version 6.12 with the nominal specimen dimensions mentioned above, see Fig. 1a. The specimen has two symmetry planes which can be exploited, therefore only one quarter of the specimen was included in the model. In addition to the symmetry boundary conditions, uniaxial and monotonic traction was prescribed on the cross section situated at the grips by restricting the node displacement on this plane to be uniform with a non zero component only in the tensile direction using a coupling equation to a dummy node [39]. The prescribed stress ramp going up to 200 MPa was then implemented by assigning an isolated force, whose magnitude is compensated by the cross sectional area, to the dummy node. Regarding the material properties, they were only assigned as elastic with data originating from a tensile test program conducted on the considered materials by Rolls Royce plc. In total, the model consisted of roughly 6000 brick elements employed with reduced integration and an approximate size of 200 μm in the gauge length volume.

Starting from the above described model, a plane crack was added by suppressing the symmetry condition over the surface at which the
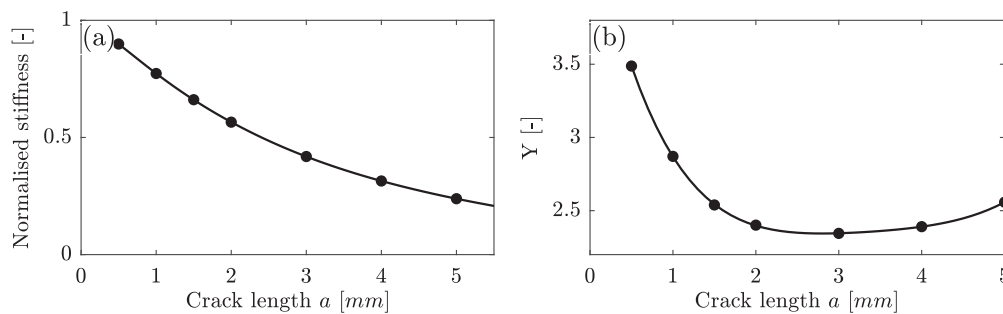
Fig. 2. Estimated dependence of the (a) normalised stiffness and (b) the geometrical factor Y on the crack length from the conducted FE simulations. Note that definition of crack length here does not include the notch depth.

crack extension was anticipated. Accordingly, a set of different models were set up, each having a plane crack of different extension ranging from 0.5 to 5 mm measured from the notch root. Around the crack tip, the mesh was refined to a spider web configuration with decreasing element size closer to the crack tip reaching the smallest size of 10 μm. The brick elements of the innermost ring were collapsed into wedge elements whose crack tip nodes were tied. In order to simulate the experiments, the stiffness of each such model was then assessed as the slope of the applied stress at the dummy node and the strain, evaluated as the node displacement at the point where the extensometer arm is placed divided by the gauge length. The result of this procedure is displayed in Fig. 2a, where the stiffness normalised to the zero crack length stiffness is plotted against the prescribed crack extension, including a polynomial fit.

Experimentally, the stiffness was evaluated in every load cycle as the slope of the stress and mechanical strain curve at the turning point of maximum stress over an interval of 80–95% of the maximum stress value. This interval corresponds to a temperature interval of 680 to 730 °C over which the elastic modulus of the material varies negligibly. The un cracked stiffness used to normalised the experimental stiffness value was taken from the initial stiffness measurement, performed prior to pre cracking, see Section 2.2.4, at the average temperature corresponding to the above stress range. Subsequently, using the polynomial expression given by the FE modelling, the stiffness was converted into a crack length and then differentiated to obtain the crack growth rate.

2.2.6. Stress intensity factor assessment method

Regarding crack growth, a conventional procedure is to relate the crack growth rate to the mode I stress intensity factor, here denoted as K_I, which is a parameter dependent on the applied stress and crack length as

$$K_I = \sigma_{max} Y(a) \sqrt{\pi a} \tag{2}$$

where σ_{max} is the nominal stress applied to the specimen and $Y(a)$ is a geometrical factor dependent on the crack length a.

The geometrical factor Y of this particular load geometry was assessed using the same set of finite element models as described above. Based on Eq. (2), the geometrical factor was computed as

$$Y(a) = \frac{\widetilde{K}_I}{\widetilde{\sigma}_{max} \sqrt{\pi a}} \tag{3}$$

where $\widetilde{K}_I$ is the stress intensity factor of the finite element model evaluated as the average stress intensity factor along the whole crack front, $\widetilde{\sigma}_{max}$ is the applied stress of 200 MPa and a is the crack length implemented in the model as mentioned above, Section 2.2.5. By varying the crack length over the set of finite element models, a functional dependence of Y was acquired, see Fig. 2b, which was fitted using a polynomial expression as similar to the stiffness curve.

As will be seen in this investigation, crack closure has an important influence on the crack growth behaviour. For this reason, the effective stress intensity factor is computed and correlated to the crack growth

rate, with the purpose of compensating for crack closure [40]. This parameter is obtained as

$$K_{I,eff} = Y(\sigma_{max} - \sigma_{op}) \sqrt{\pi a} \tag{4}$$

where σ_{max} is the nominal stress and σ_{op} is the crack opening stress which can be measured experimentally, see Sections 2.3 and 2.5, Y is the geometrical factor and a the crack length.

2.2.7. Additional thermo mechanical fatigue crack growth tests of corner cracked specimens

In order to validate the TMF crack growth experiments, additional tests performed using a different laboratory set up, but with the same test parameters, were included in the investigation. For these tests, a corner cracked specimen design with a rectangular cross section was employed, see Fig. 1b. The test piece gauge length had a 7 × 7 mm square cross section and 20 mm length, with a 0.35 mm ± 0.01 mm single edge notch machined using a diamond edge saw blade at one corner.

The TMF crack growth testing of this specimen type was undertaken using two different heating methods. The first set up comprised of an Instron 100 kN servo hydraulic test frame, utilising a Zwick CUBAS control system. A Trueheat 10 kW induction heating system was utilised to deliver rapid heating rates through a 4 mm diameter copper tube non uniform multi turn longitudinal field helical coil with an approximate external diameter of 60 mm. Rapid cooling rates were enabled through forced air cooling using four Meech pneumatic air amplifiers with their output control through proportional solenoid valves. Temperature feedback was provided through a 0.2 mm diameter N type thermocouple, spot welded at the centre of the 20 mm gauge length on an opposing face to the starter notch.

The second set up consisted of a Instron 100 kN servo-electric test frame together with a DARTEC control system. A second generation radiant lamp furnace (RLF) was designed in collaboration with Severn Thermal Solutions Ltd to generate rapid heating rates similar to that of an induction coil. The 12 kW RLF was a standard split body design with each half containing three horizontally mounted lamps. Three independently controllable heating zones allowed the accurate temperature control and profiling, whist built in internal compressed air cooling delivered the rapid cooling rates required by the complex TMF waveforms. Again temperature feedback was provided through a 0.2 mm diameter N type thermocouple, spot welded at the centre of the 20 mm gauge length on an opposing face to the starter notch.

A Dirlik control system interfaced together with the set ups described above was employed to record crack length against number of cycles readings through pulsing a 10 A signal and utilising the direct current potential drop technique. The crack length was converted into crack growth rate data by using the incremental polynomial method, as described in the ASTM 647 appendixes, standard test method for measurement of fatigue crack growth rates [41].

Similar to the single edge notched specimen described above, rigorous thermal profiling was undertaken using six 0.2 mm diameter N

Type thermocouples. These thermocouples were spot weld at the centre gauge location on each of the four rectangular specimen faces to realise the radial heating gradient. A further two thermocouples were spot welded 5 mm above and below a centre thermocouple to generate axial temperature distributions. Similarly to as described in Section 2.2.4, the authors employed the stringent temperature limits imposed by the governing TMF strain control standard [3].

The test parameters employed were the same as for the single edge notched specimen, namely a triangle waveform with $R = 0$ over a 400 750 °C temperature range with heating and cooling rates at 10 °C/s. However, due to the difference in the geometry of the specimens, a peak stress of 500 MPa were employed in order to have similar value in stress intensity factors. Regarding pre cracking, it was performed at room temperature using sinusoidal wave with $R = 0.1$, starting with propagation at 600 MPa and 4 Hz, then 550 MPa and 2 Hz and finally at 500 MPa and 1 Hz, in order to reach the starting crack length gently thereby avoiding the introduction of any residual plastic strain ahead of the crack tip. The same pre cracking procedure was used for all tested corner cracked specimens.

2.3. Crack closure stress measurement method based on specimen stiffness

Crack closure stress is vaguely defined as the nominal stress at which the crack is closed and has been demonstrated to influence the TMF crack growth rate [8,28,29]. The effect of crack closure is easily demonstrated by looking at the cyclic stress strain data in which the stiffness value significantly changes depending on whether the crack faces are in mechanical contact or not. Based on this feature, the crack closure stress was determined in the present study following a suggested procedure outlined by Palmert et al. [8].

Accordingly, the crack closure stress was assessed in terms of the ratio between the stiffness of an arbitrary cracked configuration C and the stiffness of the un cracked reference configuration C_0, where both stiffness variables depend on the instantaneous temperature and nominal stress. By this definition, C/C_0 supposedly becomes unity when the crack is completely closed, since the stiffness is expected to be the same then as for an un cracked specimen, while less than unity when the crack is open. For mathematical convenience, the stiffness ratio is transformed by the following operation

$$D = \frac{1 - C/C_0}{1 - C/C_0|_{\sigma = \sigma_{max}}} \quad (5)$$

where $C/C_0|_{\sigma = \sigma_{max}}$ is the value of the stiffness ratio at the instant of maximum nominal stress. In this way, the newly derived crack closure factor D is zero when completely closed, and unity when completely open. Note that this interpretation presupposes that the crack is completely open at maximum nominal stress, which however is expected to be true for all tests conducted in this investigation. The variation in factor D will clearly be influenced by the continuous separation of the crack faces when loaded, since the amount of partial crack closure relates to the specimen stiffness. Accordingly, the crack faces at the crack tip will be the last to separate and it is therefore motivated to associate crack closure event with the nominal stress applied when the factor D is very close to unity. For this reason, crack closure stress defined as the nominal stress at which D exceeds 0.9 in this investigation, as suggested by Palmert et al. [8].

Experimentally, crack closure was only assessed for the single edge notched specimen. The stiffness C was determined at twenty stress values regularly distributed over the loading branch of the hysteresis loop, as the slope of the stress strain curve over an interval of $\pm$ 7.5% of the maximum stress of the cycle. The temperature variation over this interval is 50 °C, over which the variation in elastic modulus is negligibly small. The reference stiffness C_0 was taken from the initial stiffness measurement, performed prior to pre cracking, see Section 2.2.4, at the average temperature corresponding to the above stress range.

2.4. Metallographic analysis of interrupted tests

A metallographic investigation was conducted on the specimens subjected to the OP and IP condition described above, namely specimen $S3$ and $S5$ in Table 1 respectively, which were interrupted at the same crack length of 4.2 mm. The specimens were then cut in order to retrieve the rectangular middle section, which in turn were cut with a cutting plane perpendicular to the crack face and parallel with the width dimension. In this way, the crack tips were studied both at the side surface of the specimen and on a plane in the centre of the notch, *i.e.* at half the thickness. The metallographic surfaces were then ground and polished using a standard program for nickel base superalloys.

The microscope equipment used were an optical microscope and a scanning electron microscope (SEM). The former was a Nikon Optiphot optical microscope and the latter a HITACHI SU-70 field emission gun SEM, equipped with a solid state 4 quadrant backscattered electron detector, using 8 and 10 kV acceleration voltage and a working distance of about 9 mm. Furthermore, energy-dispersive X-ray spectroscopy (EDS) was performed at 20 kV at a working distance of 15 mm.

2.5. Image analysis of the crack tip region

In this investigation, the deformation field ahead of the crack tip in the single edge notched specimen was measured using digital image correlation (DIC) in order to acquire a better understanding of how IP and OP loading affect the mechanical conditions at the crack tip region. For the same purpose, the displacement field was further used to assess the crack tip opening displacement.

The images were captured using a Nikon UBS29 QXC F camera mounted at a lateral viewpoint of the specimen. The images were of a size of 2592 × 1944 pixels and captured at a magnification of about 40×. The camera was positioned to view the notch from a lateral direction and images were captured every 35 s, *i.e.* twice every cycle at the instant of maximum and minimum stress. Only for a few occasions, images were captured more frequently at a frequency of 1 Hz, namely when the crack length was about 3 and 4.2 mm. No artificially added speckle pattern was utilised since the natural surface roughness was enough to acquire accurate correlation in the DIC analyses. Even so, surface oxidation was not an problem since the time between correlated images was less than required to produce significant changes in the appearance of the specimen surface. Furthermore, the view of the specimen was constantly illuminated using high power LED spots comparable to 150 W halogen light sources in order to eliminate the disturbance from the black body radiation of the specimen. An open source matlab based DIC code written by Eberl et al. at the John Hopkins University and distributed by mathworks [42], was used for the image correlation with a subset pixel size of 31 × 31 pixels.

For all conducted DIC analyses, the reference image was selected as the image taken at minimum load, *i.e.* zero applied stress, at the same load cycle as the analysed image of interest. For this reason, the displacement fields presented in this investigation are always with respect to the deformation state at zero nominal load, which is not necessarily a state of zero residual deformations.

Within the DIC software, the obtained displacement field was smoothed, using a Gaussian distribution of weights with a Gaussian kernel size of 31 control points and three smoothing passes. The smoothed displacement field was then subsequently differentiated in order to obtain the strain field. Furthermore, by assuming homogeneous temperature in the region of interest, the mechanical strain was acquired using Eq. (1), *i.e.* by subtraction of the thermal strain measured in the TMF pre test procedure.

The crack tip opening displacement (CTOD) was calculated by post processing of the DIC analyses similar to the method presented by Vasco Olmo et al. [43]. More precisely, CTOD was defined as the discontinuous jump in the field of the displacement component of the tensile direction (y-direction), at an x-position along the crack 10 μm

from the crack tip location at the instant of maximum nominal stress. The discontinuous jump in displacement was assessed by fitting a step function, namely the error function as

$$f(y) = a + b \cdot erf\left[c \cdot (y - d)\right] \qquad (6)$$

where a, b, c and d are fitting constants, to the displacement component profile in the y-direction along y-position y. From the fitted parameters, CTOD was hence defined as $2b$, since the total step height of the error function is 2. This procedure was performed over a range of x-positions along the crack, yielding a crack opening profile along the crack, from which the value at a 10 μm distance from the crack tip was determined.

Due to the difficulty to accurately identify the crack tip location by visual inspection systematically, a special criteria was employed to assess the pixel coordinates of the crack tip in the images. Since the y-coordinate of the crack is conveniently assessed by the above fit, *i.e.* as the d parameter [43], the real difficulty was to assess the x-coordinate. To this end, this location was defined as the x-position along the crack at which the slope of the fitted step function, *i.e.* $\frac{df}{dy}|_{y=0} = \frac{2}{\sqrt{\pi}} bc$, falls below a critical value taken as 0.1. This criteria is well motivated since a too low value of the slope indicates that there is no discontinuity in the displacement field. The particular value of 0.1 was chosen based on agreement with manual inspections of crack tips in images.

In addition, based on the measured CTOD, the crack closure stress was measured as the stress at which the CTOD exceeds 1 μm. To increase the reliability of this measurement, the average stress CTOD curve over three subsequent cycles was considered. The reason for taking this particular value was simply that it roughly corresponded to the minimum detectable opening in view of the scatter over these three cycles. The crack opening stress was only assessed at crack length of three millimetres in all tests, which were used as a representative value for the whole tests.

2.6. Modelling of the deformation behaviour at the crack tip

As a complement to the DIC measurement, finite element (FE) modelling of the displacement field around the crack tip in the single edge notched specimen was performed. The intention with this work was to complement the DIC measurements as well as acquire more detailed information about the local strain ahead of the crack tip and the crack opening.

To this end, the same specimen model as used for the compliance method and stress intensity factor computation was employed, except for higher degree of mesh refinement at the crack tip corresponding to a smallest element size of 5 μm at the crack tip. However, rather than restricting the behaviour to purely elastic, the material was given an ideal plastic von Mises behaviour [39]. Hence, the effective von Mises stress at yield, as well as the elastic modulus, was assessed as the temperature dependent mechanical properties acquired from a series of tensile tests at different temperatures performed by Rolls Royce plc. This is a simplified approach but is motivated in view of the low rate of hardening seen in tensile tests and the ensuing results in agreement with experimental data as demonstrated later in Section 3.2. Moreover, the employed temperature dependent thermal expansion coefficients were calculated from the thermal strain measured in the TMF pre test procedure.

The boundary conditions were applied in the same way as when performing the compliance method described in Section 2.2. Similarly, the same set of different models were set up, each having a plane crack of different extension ranging from 0.5 to 5 mm measured from the notch root. However, in order to represent the cyclic history associated with the cyclic loading in the experiments, each model was cycled between zero and 210 MPa over three cycles. The load values were chosen to be the same as in the experiments, *i.e.* specimen $S3$ and $S5$ in Table 1. Additional cycles did not have any further significant effect due to the ideal plastic material behaviour. Moreover, time dependent

uniform temperature fields were applied with the same cyclic variations and magnitudes as in the experimental OP and IP cycling, *i.e.* between 400 °C and 750 °C.

In order to have consistency with the DIC analyses, the strain fields acquired from the FE simulations were taken with reference to the deformation state at zero nominal load of the same cycle, using available tools in Abaqus [39]. Furthermore, the computed thermal strain was subtracted from this strain field output, in agreement with Eq. (1), in order to acquire the mechanical strain field. A definition of CTOD consistent with the DIC post processing was also employed, namely as the interpolated node displacement in the y-direction at the position of 10 μm from the crack tip location at the instant of maximum nominal stress.

3. Results and discussion

3.1. Investigation of the effect of crack closure

In a wide context, crack closure has been demonstrated to affect the fatigue crack growth rate in metallic materials [40,44]. Regrading the present material type and load condition, the origin to crack closure has been attributed to a number of phenomena including plasticity [8,20,45,46], roughness [21] and oxide induced [7,12] crack closure. However, without particular knowledge of the exact closure mechanism, recent studies [8,28–30] have demonstrated that variations in crack growth rate caused by altering the load ratio and temperature cycle are accounted for by compensating the stress intensity factor range or the cyclic J-integral with respect to crack closure, *i.e.* Eq. (4) in Section 2.2. For this reason, the effect of crack closure is investigated in the present study to see whether it may explain the distinction between in-phase (IP) and out-of-phase (OP) cycling.

Experimental determination of crack closure is however a subject of controversy. In this investigation, two methods were employed, namely by direct visual observation supported by digital image correlation (DIC) and a method based on the measurement of the compliance variation caused by crack closure, both explained in Sections 2.5 and 2.2 respectively. For the latter method, the compliance variation over a given load cycle is converted to an opening parameter D, which by its definition attains zero when completely closed and unity when completely open. Accordingly, the crack opening stress σ_{op} can then be defined as a critical value of D, here selected as 0.9, see Section 2.3.

Fig. 3 compares the outcome when using the two different methods to assess the degree of crack closure. In Fig. 3a, the crack tip opening displacement (CTOD) measured using DIC is plotted as a function of stress for one OP cycle and an IP cycle which occurred at a crack length of about 3 mm in both cases. For the same OP and IP cycle, the crack opening parameter D is plotted as a function of stress in Fig. 3b. In the former figure, crack opening is interpreted as the instant when CTOD exceeds a limit value, chosen as 1 μm, and in the former, when the opening parameter exceeds 0.9, as motivated in Sections 2.5 and 2.2 respectively.

Interestingly, it is indicated that the two methods do not yield consistent values of the crack opening stress σ_{op}. While the compliance method results in a significant difference in crack opening stress between OP and IP, the DIC method asserts that the values are adjacent and underestimated. The reason for this is mainly believed to be that the critical value of the opening parameter 0.9, is not strict enough. However, due to limitations of accuracy of measurement of the specimen compliance, it is meaningless to select a higher value, *e.g.* 0.95, since such small deviation from unity is comparable in magnitude to the measurement error of the opening parameter. Nevertheless, the DIC method is argued to be more reliable since the method is based on the local deformation events at the crack tip, rather than a macroscopic variable such as the specimen compliance.

Using the crack opening stress acquired using the DIC method, thermo mechanical faitgue (TMF) crack growth rate is correlated with
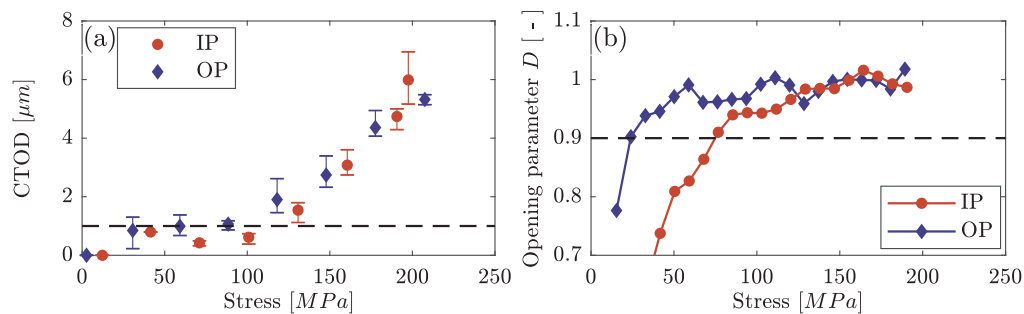
Fig. 3. (a) Crack tip opening displacement (CTOD) and (b) opening parameter D derived from the specimen compliance, as a function of applied stress for one IP and one OP cycle at a crack length of about 3 mm in both cases. The test parameters were 400–750 °C, $R = 0$ and $\sigma_{max} = 210$ MPa, and the tested specimens were $S3$ and $S5$, presented in Table 1, for the OP and IP test respectively. In (a), the average, maximum and minimum value of CTOD over three subsequent load cycle.s are displayed.
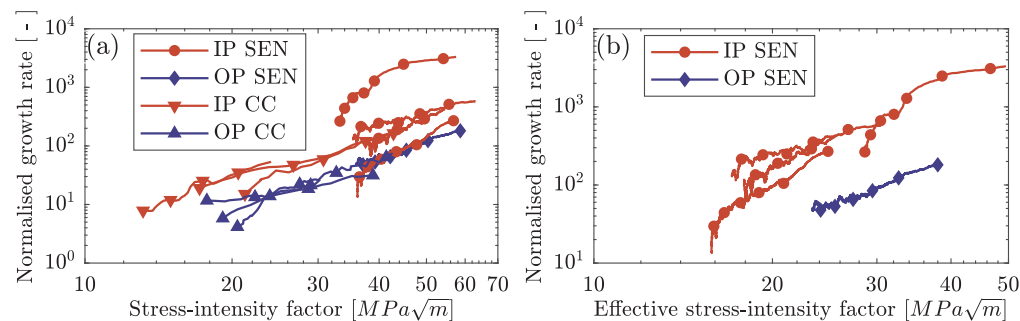

Fig. 4. Fatigue crack growth rate as a function of (a) stress-intensity factor and (b) effective stress intensity factor in the single edge notched (SEN) and corner cracked (CC) specimen subjected to OP and IP TMF loading with 400–750 °C and $R = 0$. All conducted TMF test are included, however they are only differentiated if the test is OP or IP. The SEN specimen tested in IP have been subjected to different pre-crack procedures, as presented in Table 1. The effective stress intensity factor is calculated according to Eq. (4) for which the stress opening stress is acquired using the DIC method, see Section 2.5.

respect to the stress intensity factor and the effective stress intensity factor for which crack closure is compensated as described in Section 2.2.6, see Fig. 4. Surprisingly, the variations seen in the IP tests of the single edge notched (SEN) specimen in Fig. 4a are eliminated by compensating for crack closure. A similar observation was made in the investigation by Palmert et al. [8] in which isothermal and IP crack growth tests with various load ratios and durations of dwell on a single crystal nickel base alloy, collapsed into a single curve when adjusted for crack closure. In contrast, the variation of growth rates seen in here is likely to originate from the difference in the pre cracking procedure, in view of the low amount of variation seen for the corner crack (CC) specimen for which the pre crack procedure was not varied. Thus, it is concluded that the pre cracking procedure, *i.e.* the choice of load ratio and whether the pre crack cycling is thermo mechanical or conducted at room temperature, does not explicitly affect the crack propagation rate. Rather, it has an implicit effect which is entirely accounted for by the influence of crack closure on fatigue crack propagation.

It is noted that for test conducted with the same pre-crack procedure, the crack opening stress is lower in OP than in IP, see Fig. 3a. This is in line with a recent study of a temperature dependent yield strip model intended for TMF crack growth [45], which has indicated that crack closure is more pronounced in IP compared to OP. However, it is not evident why the difference in pre-cracking procedure has such a significant effect on the crack opening level. It is suggested that the different pre cracking procedures, see Table 1, have caused different amount of residual plastic deformation in the notch which plausibly could affect the degree of subsequent crack closure. Unfortunately, no detailed information about the residual strain field is available, hence this proposition cannot be confirmed at present.

Looking at the crack growth behaviour of both specimen types in Fig. 4, it is seen that IP loading results in a distinctly higher crack growth rate compared to OP loading. This is expected since in IP the

crack is exposed to the maximum load at the same instant of maximum temperature, during which the material is less prone to withstand high stresses and oxidation effects. Furthermore, based the results of the SEN specimen, it is concluded that crack closure effect is of importance in assessing the fatigue crack growth rate. However, it does not single handedly account for the distinction between growth rates in OP and IP loading.

3.2. Analysis of the crack tip deformation behaviour

A general aspect which may account for the differences between in-phase (IP) and out-of-phase (OP) load conditions, is the stress-strain state in the region ahead of the crack tip. Some authors have for instance argued that inelastic creep deformation at the crack tip may potentially contribute to increased crack growth rates in nickel base superalloys [7,11,12,14,15,19,20,47]. Furthermore, it is also expected that the crack tip stress strain state affects the diffusion of oxygen [9,10,16,31], whose presence has been demonstrated to severely affect the fatigue crack growth rate based on crack growth test under air and vacuum conditions [9–17]. Thus, even in the absence of sustained loads and an oxidising atmosphere, different thermo mechanical cycles may impose different crack tip stress strain states due to the temperature-dependence of the mechanical constitutive behaviour of the material. This is an important aspect which must be clarified in order to fully distinguish IP and OP load conditions.

Using digital image correlation (DIC) technique, the above presumption is affirmed, see Fig. 5a and b. The figure shows the mechanical strain field ahead of the crack tip at maximum applied stress of 210 MPa at one OP and one IP cycle which occurred at a crack length of about 3 mm. Even though the differences are small, the IP cycle is seen to impose a higher mechanical straining in the crack tip region. This is further supported by the conducted finite element (FE) simulations
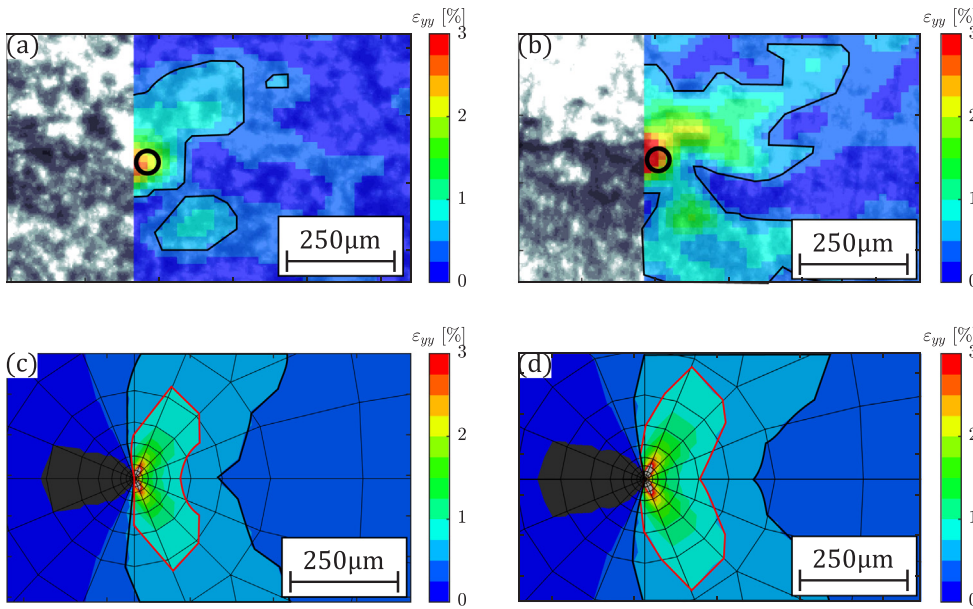
Fig. 5. Mechanical strain field in the tensile direction measured using DIC in (a) an OP and (b) IP cycle, as well as simulated by finite element (FE) analysis, (c) and (d) for the OP and IP cycle respectively. The mechanical strain is measured at the maximum cyclic stress with reference to the minimum cycle stress of zero MPa at the cycle corresponding to a crack length of 3 mm in both the experiments and FE simulations. The test parameters were 400–750 °C, $R = 0$ and $\sigma_{max} = 210$ MPa, and the studied specimens were $S3$ and $S5$, presented in Table 1, for the OP and IP test respectively. In (a) and (b), the mechanical strain field at maximum stress is averaged over three subsequent cycles during which the movement of the crack tip location, as marked out by the circle, is negligible. To ease the distinction between the figures, level curves corresponding to the uniaxial yield strain, which is about 0.5% over the temperature range 400–750 °C, and 0.75%, *i.e.* $\varepsilon_{yy} = \sigma_y/E \cong 0.5\%$ in black and $\varepsilon_{yy} = 0.75\%$ in red, are included. (For interpretation of the references to color in this figure legend, the reader is referred to the web version of this article.)

presented in Fig. 5c and d, which manifest a similar appearance in the mechanical strain field, as well as a small difference between the OP and IP cycle. Thus, there is consistent theoretical and experimental support to argue that IP cycling results in higher deformation at the crack tip region compared to OP cycling.

It should be remembered that the FE model in Figs. 5c and d does not incorporate the effect of crack closure. Thus, the FE simulations only reflect the difference originating from the effect of a phase shift in the temperature cycle, without the eventual influence of crack closure. Consequently, strain localisation at the crack tip occurs at all stress levels in the FE model, even though it is not intuitively expected in reality for stress levels below the crack opening stress. On the other hand, crack closure occurs almost concurrently in the considered OP and IP cycle, see Fig. 3a. Therefore, the difference seen in Fig. 5a and b is mainly associated with the effect of the temperature cycle on the thermo mechanical constitutive behaviour.

The difference in mechanical straining between IP and OP in absence of crack closure, is attributed to the temperature dependence of the yield strength. Clearly, the material is at maximum temperature at maximum stress, during which the yield strength is lower compared to at minimum temperature. As a result, the crack tip is subjected to a higher degree of inelastic deformation in contrast to an OP cycle, for which inelastic deformation is better resisted thanks to the higher yield strength at lower temperatures.

A larger crack tip deformation in the IP case is also reflected in the measurement of the crack tip opening displacement (CTOD), see Fig. 3a, in which CTOD is shown to be larger in IP compared to OP for the same applied stress and crack length. This is further illustrated in

Fig. 6a, in which CTOD measured by DIC is plotted as function of crack length. Effectively, the crack tip opens up more at maximum stress in IP compared to OP for the major part of the tests.

In Fig. 6a, CTOD acquired from the FE simulations is included as well, which demonstrates the overestimation of the experimentally measured values. The discrepancy is again argued to be due to the absence of crack closure in the FE model. To compensate for this, an alternative definition of CTOD is attempted in which CTOD is assessed as

$$\delta = \delta^{FE}|_{\sigma=\sigma_{max}} - \delta^{FE}|_{\sigma=\sigma_{op}} \tag{7}$$

where δ^{FE} is the closure-free CTOD computed in the FE model, σ_{max} is the maximum stress of the cycle and σ_{op} is the crack opening stress determined using DIC. This expression is a simple empirical estimate similar to the proposition given by Donahue et al. [48], and accounts for the effect of crack closure on CTOD by considering the crack opening relative to the value at the crack opening stress σ_{op}. Based on this measure, improved agreement with experimentally measured values is obtained, see Fig. 6b, even though CTOD in OP is still overestimated, which much likely is due to the absence of hardening behaviour in the FE model. Nevertheless, both experiments and the FE simulations indicate that IP loading results in higher crack tip opening compared to OP, also when the effect of crack closure is included.

Based on the above observation, it is well motivated to suggest that the higher crack growth rate in IP, as demonstrated in Fig. 4b, may originate from more severe mechanical load conditions at the crack tip region. To validate this proposition, it is argued that CTOD is a suitable parameter to relate to crack tip deformation, since theoretically, a
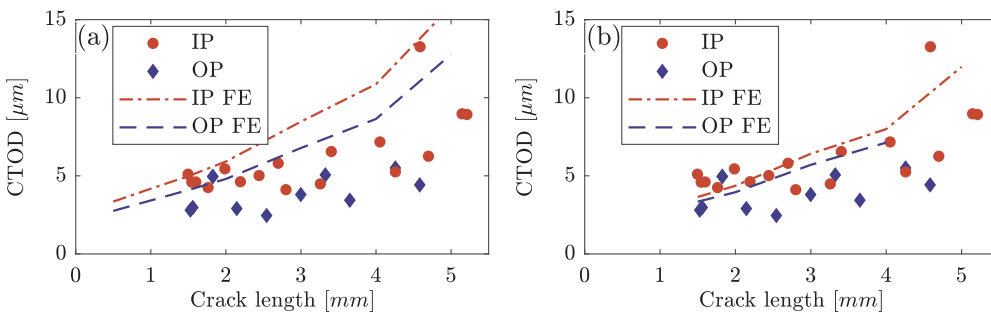

Fig. 6. Crack tip opening displacement (CTOD) as a function of crack length measured by DIC and modelled using FE and Eq. (7). In (a) the experimentally measured CTOD is compared with CTOD measured in the FE directly, see Section 2.6, while in (b), the measured CTOD is compared to the estimate given by Eq. (7). The test parameters were 400–750 °C, $R = 0$ and $\sigma_{max} = 210$ MPa, and the tested specimens were $S3$ and $S5$, presented in Table 1, for the OP and IP test respectively.
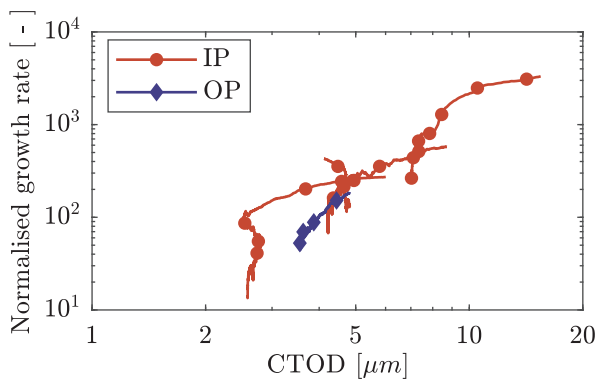
Fig. 7. Fatigue crack growth rate in the single edge notched specimen as a function of CTOD measured using DIC, see Section 2.5, when subjected to TMF cycling for which the test parameters were 400–750 °C, $R = 0$ and $\sigma_{max} = 210$ MPa.

higher CTOD can only be accommodated through higher straining of the region ahead of the crack tip. The argument is also supported by the investigation by Eckmann and Schweizer [20], in which damage evolution ahead of the crack is correlated with the crack mouth opening, which is similar parameter related to how much a crack is open.

Accepting this premise, the correlation between crack growth rate and CTOD is made as similar to previous investigations [38,48–50], see Fig. 7. Intriguingly, this correlation demonstrates the approaching of the IP and OP curves compared to Fig. 4b, which suggests that the fatigue crack growth rate in OP and IP are similar when compared at equivalent mechanical conditions at the crack tip. In other words, the crack growth rate seems to be dominated by the amount of crack tip deformation and opening which is caused during a given cycle, including the effects of crack closure and the constitutive behaviour of the material.

The above demonstration suggests that oxidation plays a minor role in distinguishing the mechanisms of crack growth in OP and IP loading, in contrast to previous suggestions regarding isothermal dwell fatigue [18] and TMF conditions [6,7]. However, as discussed in the next

section, oxygen is known to accelerate the crack growth rate at elevated temperatures. Therefore, it is emphasised that crack growth is not independent of an oxidising atmosphere. Rather, it is proposed that the difference in the effect of oxygen between IP and OP loading is small for the tested material, as further discussed in the next section.

3.3. Metallographic investigation of the crack tip region

The results of the previous sections suggest that the effective inphase (IP) and out of phase (OP) TMF crack growth in RR1000 is mainly controlled by the deformation caused at the crack tip. On the other hand, many investigators have pointed out that crack tip oxidation clearly influences the crack growth rate at constant elevated temperature for nickel base superalloys. In particular, it has been convincingly demonstrated that the effect of oxygen accelerates the isothermal crack growth rate by performing tests at different partial pressures of oxygen [9–17], including investigations on RR1000 [11,14,16]. Furthermore, grain boundary oxidation ahead of the crack tip has been reported in Inconel 718 [19], as well as in RR1000 [14,22,23], under sustained load conditions. Clearly, there is a potential influence of material related aspects, such as the influence of the microstructure and oxidation at the high stressed crack tip region, which requires attention in view of the results of the previous sections.

Fig. 8 displays the cross sectional appearance of the primary crack tip in the centre of the specimen, *i.e.* middle position of the crack front, for the OP and IP test interrupted at a crack length of roughly 4.2 mm in both specimens. The figure also includes energy dispersive X ray spectroscopy (EDS) results of the same area with respect the chemical presence of oxygen. Clearly, oxygen is present in the crack as expected in both the OP and IP specimen. However, the analysis, including the visual inspection of the SEM images, does not indicate a significant distinction regarding the role of oxides between the two crack tips.

These observations are in agreement with previous investigations of fatigue crack tip oxidation in RR1000 subjected to sustained loads of $K_{I,max}$ equal to 20 MPa $\sqrt{m}$ during 10 min [51,52], and of ΔK equal to 17 and 30 MPa $\sqrt{m}$ during one hour [18] at 700 °C in air, for which no oxygen were identified ahead of the crack tip. On the other hand, longer
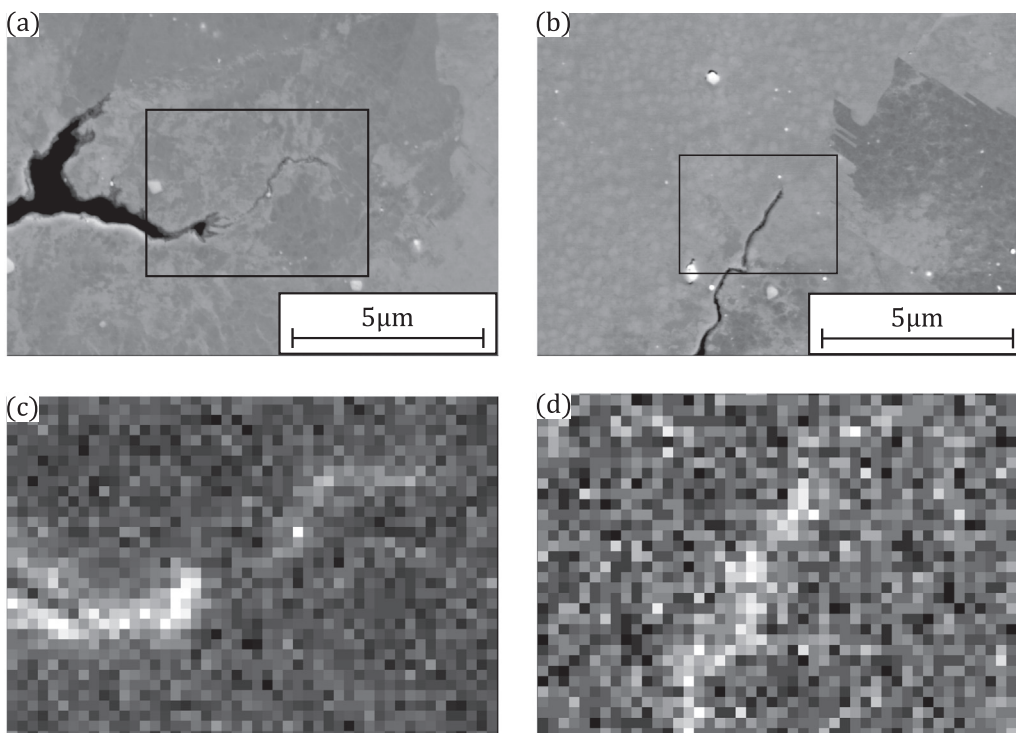

Fig. 8. Backscattered scanning electron microscopy (SEM) images of the primary crack tip at a crack length of roughly 4.2 mm in the specimen subjected to (a) OP and (b) IP, as well as EDS analyses of the same areas with respect to chemical presence of oxygen in (c) OP and (d) IP. The SEM images are captured using 10 kV acceleration voltage, 9 mm working distance and with 10 k magnification.
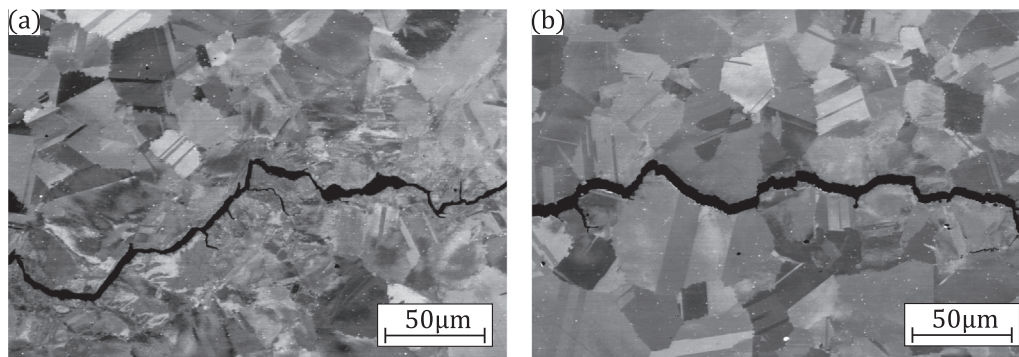
Fig. 9. Backscattered scanning electron microscopy (SEM) images of the crack path in (a) OP, showing transgranular growth, and (b) IP, showing mixed inter and transgranular morphology. The SEM images are captured using 8 kV acceleration voltage, 9 mm working distance and with 500 magnification.

dwell times have shown to yield traces of isolated oxides ahead of the crack tip in RR1000 [14,22,23]. In the present study, the specimens were only subjected to temperature in the range of 700–750 °C during 10 s, coincident with maximum load only for the IP tests. Thus, in view of the tested thermo mechanical load cycle of 70 s cycle period, it is not unexpected that the time is insufficient to cause significant crack tip oxidation. This point clearly favours the argument that the assistance of oxidation does not account for the difference between IP and OP crack growth rates in RR1000, as suggested in the previous section.

On the other hand, the above argument is opposed by the observed difference in crack path morphology between OP and IP crack growth. In agreement to what is often reported for nickel base superalloys [6,7,24], the conducted IP tests tend to manifest intergranular growth while OP is more transgranular, see Fig. 9, which is consistent with the general observation of increased tendency for intergranular growth with increasing temperatures [15,25–27] and dwell times [14,15,53] under isothermal conditions. More importantly, it is also reported that the propensity of intergranular growth morphology decreases with decreasing partial pressure of oxygen [9,11,12,14], which indicates a dependency of the crack growth mechanism on the presence of oxygen. Thus, based on the crack path morphology, the influence of oxygen on the distinction between IP an OP crack growth in RR1000 cannot be completely ruled out at this point.

Another observable feature in Fig. 9 is the difference in the caused deformation in the wake of the growing crack. Based on the achieved electron channelling contrast [18,54], the IP case demonstrates low amount of deformation, except for the few grains which have failed trangranularly, see Fig. 9b, whereas the OP case indicates severe deformation, see Fig. 9a. Thus, it appears as if plastic deformation associated with the crack tip is accommodated by plastic deformation within the grain in OP crack growth, while deformation in terms of grain boundary sliding seems more justified in IP crack growth. By some investigators [55,56], grain boundary sliding ahead of the crack tip has been suggested to complement environmentally assisted intergranular cracking of nickel base superalloys. However, it has also recently been demonstrated that grain boundary sliding occurs even under vacuum, above 700 °C when subjected to tensile and creep load conditions [57–60]. Thus, this indicates that oxygen is not necessarily needed to cause intergranular deformation at elevated temperatures. Consequently, it is possible that the difference in crack path morphology between OP and IP is a result of changes in the deformation behaviour of the microstructure between 400 °C and 750 °C, regardless of the role of oxygen.

4. Conclusions

- Based on the adjacent correlations of both IP and OP crack growth rates to the crack tip opening displacement, and the observed absence of oxygen ahead of the crack tip, it is proposed that the

difference between IP and OP TMF crack growth rate in coarse grained RR1000 originates from the mechanical conditions at the crack tip region, rather than environmental effects. This is supported by digital image correlation analyses of the mechanical strain field at the crack tip, which demonstrate that IP cycling leads to larger crack tip deformation compared to OP at the same crack length and load parameters (σ_{max} = 210 MPa, R = 0 and T = 400–750 °C). Moreover, finite element modelling suggests that the observed differences in crack tip deformation and opening arise from the effect of crack closure and the temperature dependence of the constitutive behaviour of the material.

- For the tested single edge notched specimen, crack closure assessed in terms of a crack opening stress σ_{op}, is highly dependent of the pre cracking procedure, *i.e.* the choice of load ratio and whether the pre crack cycling is thermo mechanical or conducted at room temperature. However, the effective crack growth rate adjusted for crack closure, is independent of pre cracking procedure.

Declaration of Competing Interest

The authors declare that they have no known competing financial interests or personal relationships that could have appeared to influence the work reported in this paper.

Acknowledgement

References

[1] Advisory council for aviation research and innovation in Europe.
[2] Koff BL, Fellow A, Gardens PB. Gas turbine technology evolution: a designers perspective. J Propul Power 2004;20(4):577–95.
[3] Metallic materials — Fatigue testing — Strain-controlled thermomechanical fatigue testing method, Tech. rep.; 2011.
[4] McKnight RL, Laflen JH, Spamer GT. Turbine blade tip durability analysis. Tech. rep., CR 165268. National Aeronautics and Space Administration; 1982.
[5] Sehitoglu H. Thermal and thermomechanical fatigue of structural alloys. Fatigue Fract 1996;19:527–56.
[6] Pretty C, Whittaker M, Williams S. Crack growth of a polycrystalline nickel alloy under TMF loading. Adv Mater Res 2014;891–892:1302–7.
[7] Pretty C, Whitaker M, Williams S. Thermo-mechanical fatigue crack growth of RR1000. Materials 2017;10(1):34.
[8] Palmert F, Moverare J, Gustafsson D. Thermomechanical fatigue crack growth in a single crystal nickel base superalloy. Int J Fatigue 2019;122:184–98.
[9] Andrieu E, Molins R, Ghonem H, Pineau A. Intergranular crack tip oxidation mechanism in a nickel-based superalloy. Mater Sci Eng A 1992;154(1):21–8.
[10] Pfaendtner J, McMahon C. Oxygen-induced intergranular cracking of a Ni-based alloy at elevated temeratures - an example of dynamic embrittlement. Acta Mater 2001;49:3369–77.
[11] Knowles DM, Hunt DW. The influence of microstructure and environment on the crack growth behavior of powder metallurgy nickel superalloy RR1000. Metall

Mater Trans A: Phys Metall Mater Sci 2002;33(10):3165–72.

[12] Osinkolu GA, Onofrio G, Marchionni M. Fatigue crack growth in polycrystalline IN 718 superalloy. Mater Sci Eng A 2003;356(1–2):425–33.

[13] Winstone MR, Brooks JW. Advanced high temperature materials: aeroengine fatigue. High Temp Fatigue 2008;20(1–2):15–24.

[14] Li HY, Sun JF, Hardy MC, Evans HE, Williams SJ, Doel TJ, et al. Effects of microstructure on high temperature dwell fatigue crack growth in a coarse grain PM nickel based superalloy. Acta Mater 2015;90:355–69.

[15] Jiang R, Everitt S, Gao N, Soady K, Brooks JW, Reed PA. Influence of oxidation on fatigue crack initiation and propagation in turbine disc alloy N18. Int J Fatigue 2015;75:89–99.

[16] Jiang R, Reed PA. Critical assessment 21: oxygen-assisted fatigue crack propagation in turbine disc superalloys. Mater Sci Technol (United Kingdom) 2016;32(5):401–6.

[17] Jiang R, Bull DJ, Proprentner D, Shollock B, Reed PA. Effects of oxygen-related damage on dwell-fatigue crack propagation in a P/M Ni-based superalloy: from 2D to 3D assessment. Int J Fatigue 2017;99:175–86.

[18] Yu S, Li H, Hardy M, McDonald S, Bowen P. Mechanisms of dwell fatigue crack growth in an advanced nickel disc alloy RR1000. MATEC Web of Conf 2014;14:03002.

[19] Gustafsson D, Moverare JJ, Johansson S, Simonsson K, Hörnqvist M, Mnsson T, et al. Influence of high temperature hold times on the fatigue crack propagation in Inconel 718. Int J Fatigue 2011;33(11):1461–9.

[20] Eckmann S, Schweizer C. Characterization of fatigue crack growth, damage mechanisms and damage evolution of the nickel-based superalloys MAR-M247 CC (HIP) and CM-247 LC under thermomechanical fatigue loading using in situ optical microscopy. Int J Fatigue 2017;99:235–41.

[21] McCarver JF, Ritchie RO. Fatigue crack propagation thresholds for long and short cracks in René 95 Nickel-base superalloy. Mater Sci Eng 1982;55(1):63–7.

[22] Kitaguchi HS, Li HY, Evans HE, Ding RG, Jones IP, Baxter G, et al. Oxidation ahead of a crack tip in an advanced Ni-based superalloy. Acta Mater 2013;61(6):1968–81.

[23] Kitaguchi HS, Moody MP, Li HY, Evans HE, Hardy MC, Lozano-Perez S. An atom probe tomography study of the oxide-metal interface of an oxide intrusion ahead of a crack in a polycrystalline Ni-based superalloy. Scripta Mater 2015;97:41–4.

[24] Hyde CJ, Sun W, Hyde TH. An investigation of the failure mechanisms in high temperature materials subjected to isothermal and anisothermal fatigue and creep conditions. Procedia Eng 2011;10:1157–62.

[25] Daus F, Li HY, Baxter G, Bray S, Bowen P. Mechanical and microstructural assessments of RR1000 to IN718 inertia welds – effects of welding parameters. Mater Sci Technol 2007;23(12):1424–32.

[26] Jiang R, Everitt S, Lewandowski M, Gao N, Reed PA. Grain size effects in a Ni-based turbine disc alloy in the time and cycle dependent crack growth regimes. Int J Fatigue 2014;62:217–27.

[27] Xu C, Yao ZH, Dong JX. The sharp drop in fatigue crack growth life at a critical elevated temperature for a PM Ni-based superalloy FGH97. Mater Sci Eng A 2019;761(February).

[28] Jacobsson L, Persson C, Melin S. Thermo-mechanical fatigue crack propagation experiments in Inconel 718. Int J Fatigue 2009;31(8–9):1318–26.

[29] Ewest D, Almroth P, Leidermark D, Simonsson K, Sjödin B. Fatigue crack propagation in a ductile superalloy at room temperature and extensive cyclic plastic flow. Int J Fatigue 2015;80:40–9.

[30] Ewest D, Almroth P, Sjödin B, Leidermark D, Simonsson K. Isothermal and thermomechanical fatigue crack propagation in both virgin and thermally aged Haynes 230. Int J Fatigue 2019;120(October 2018):96–106.

[31] Evans HE, Li HY, Bowen P. A mechanism for stress-aided grain boundary oxidation ahead of cracks. Scripta Mater 2013;69(2):179–82.

[32] McEvily AJ, Gonzalez Velazquez J. Fatigue crack tip deformation. Metall Trans A 1992;23(8):2211–21.

[33] Hardy M, Zirbel B, Shen G, Shenkar R. Developing damage tolerance and creep resistance in a high strength nickel alloy for disc applications. Superalloys 2004;2004:83–90.

[34] Mitchell R, Lemsky J, Ramanathan R, Li H, Perkins K, Connor L. Process development and microstructure and mechanical property evaluation of a dual microstructure heat treated advanced nickel disc alloy. Superalloys 2008;2008:347–56.

[35] Mitchell R, Hardy M, Preuss M, Tin S. Development of γ morphology in P/M rotor disc alloys during heat treatment. Superalloys 2004;2004:361–70.

[36] Collins DM, Heenan RK, Stone HJ. Characterization of gamma prime (γ) precipitates in a polycrystalline nickel-base superalloy using small-angle neutron scattering. Metall Mater Trans A 2011;42(1):49–59.

[37] Ewest D, Almroth P, Sjödin B, Simonsson K, Leidermark D, Moverare J. A modified compliance method for fatigue crack propagation applied on a single edge notch specimen. Int J Fatigue 2016;92:61–70.

[38] Norman V, Skoglund P, Leidermark D, Moverare J. The transition from micro- to macrocrack growth in compacted graphite iron subjected to thermo-mechanical fatigue. Eng Fract Mech 2017;186:268–82.

[39] Abaqus, Abaqus/CAE user's manual, ver. 6.12; 2012.

[40] Elber W. The significance of fatigue crack closure. Damage tolerance in aircraft structures. ASTM International; 1971.

[41] ASTM, Standard Test Method for Measurement of Fatigue Crack Growth Rates, Tech. rep.; 2014.

[42] Eberl C, Thompson R, Gianola D. Matlab-based DIC code, version 2. Matlab's File Exchange; 2015.

[43] Vasco-Olmo JM, Díaz FA, Antunes FV, James MN. Experimental evaluation of CTOD in constant amplitude fatigue crack growth from crack tip displacement fields. Frattura ed Integrita Strutturale 2017;11(41):157–65.

[44] Suresh S. Fatigue of materials, second ed. Cambridge: Cambridge University Press; 1998.

[45] Fischer C, Schweizer C, Seifert T. Assessment of fatigue crack closure under in-phase and out-of-phase thermomechanical fatigue loading using a temperature dependent strip yield model. Int J Fatigue 2015;78:22–30.

[46] Fischer C, Schweizer C, Seifert T. A crack opening stress equation for in-phase and out-of-phase thermomechanical fatigue loading. Int J Fatigue 2016;88:178–84.

[47] Addison DA, Tucker JD, Siegmund T, Tomar V, Kruzic JJ. Cyclic and time-dependent crack growth mechanisms in Alloy 617 at 800 C. Mater Sci Eng A 2018;737(July):205–12.

[48] Donahue RJ, Clark HM, Atanmo P, Kumble R, McEvily AJ. Crack opening displacement and the rate of fatigue crack growth. Int J Fract Mech 1972;8(2):209–19.

[49] Liu HW. Fatigue crack growth by crack tip cyclic plastic deformation: the unzipping model. Int J Fract 1989;39(1–3):63–77.

[50] Antunes FV, Branco R, Prates PA, Borrego L. Fatigue crack growth modelling based on CTOD for the 7050–T6 alloy. Fatigue Fract Eng Mater Struct 2017;40(8):1309–20.

[51] Viskari L, Hörnqvist M, Moore KL, Cao Y, Stiller K. Intergranular crack tip oxidation in a Ni-base superalloy. Acta Mater 2013;61(10):3630–9.

[52] Hörnqvist M, Viskari L, Moore KL, Stiller K. High-temperature crack growth in a Ni-base superalloy during sustained load. Mater Sci Eng A 2014;609:131–40.

[53] Moverare JJ, Gustafsson D. Hold-time effect on the thermo-mechanical fatigue crack growth behaviour of Inconel 718. Mater Sci Eng A 2011;528(29–30):8660–70.

[54] Gutierrez-Urrutia I, Zaefferer S, Raabe D. Coupling of electron channeling with EBSD: toward the quantitative characterization of deformation structures in the sem. Jom 2013;65(9):1229–36.

[55] Chen X, Yang Z, Sokolov MA, Erdman DL, Mo K, Stubbins JF. Effect of creep and oxidation on reduced fatigue life of Ni-based alloy 617 at 850 °c. J Nucl Mater 2014;444(1–3):393–403.

[56] Németh AA, Crudden DJ, Armstrong DE, Collins DM, Li K, Wilkinson AJ, et al. Environmentally-assisted grain boundary attack as a mechanism of embrittlement in a nickel-based superalloy. Acta Mater 2017;126:361–71.

[57] Soula A, Renollet Y, Boivin D, Pouchou JL, Locq D, Caron P, et al. Analysis of high-temperature creep deformation in a polycrystalline nickel-base superalloy. Mater Sci Eng A 2009;510–511:301–6.

[58] Walley JL, Wheeler R, Uchic MD, Mills MJ. In-situ mechanical testing for characterizing strain localization during deformation at elevated temperatures. Exp Mech 2012;52(4):405–16.

[59] Carter JL, Kuper MW, Uchic MD, Mills MJ. Characterization of localized deformation near grain boundaries of superalloy René-104 at elevated temperature. Mater Sci Eng A 2014;605:127–36.

[60] Pataky GJ, Sehitoglu H. Experimental methodology for studying strain heterogeneity with microstructural data from high temperature deformation. Exp Mech 2015;55(1):53–63.